

From Accounting to Coordination: A Virtual Water-Aware Electricity–Computation–Water Nexus Framework for Data Center Dispatch

Haiyang You, Chengwei Lou, Jin Zhao, *Member, IEEE*, Yue Zhou, *Member, IEEE*, Lu Zhang, *Senior Member, IEEE*, Jin Yang, *Senior Member, IEEE*

Abstract—The expansion of data centers (DCs) drives a sustained increase in electricity demand and associated water withdrawals at generation sites. These withdrawals occur at generation sites and are virtually allocated to demand based on network power flows. Consequently, the actual water footprint of a specific load varies dynamically with generation dispatch and network conditions. Existing approaches typically rely on static statistical accounting to quantify these water footprints. However, these static methods fail to capture how dispatch optimization and workload relocation dynamically affect water withdrawals. As a result, these static statistical accounting remain decoupled from the optimization process, rendering them incapable of guiding workload relocation or power dispatch to mitigate water stress. To address this limitation, this paper develops an operational electricity–computation–water (ECW) nexus framework that internalizes virtual water impacts directly into power system dispatch. The framework represents dispatch optimization as a differentiable optimization layer embedded within a deep learning architecture, enabling efficient end-to-end learning of coordination policies while preserving operational feasibility. Combined with fixed-point coordination, the framework enforces consistency between virtual water attribution and physical generation side withdrawals. Case studies on the IEEE 30-bus and 118-bus test systems demonstrate reliable convergence, exact power–water consistency, and reductions of approximately 3–5% in generation-related freshwater withdrawals under water-constrained conditions.

Index Terms—Virtual water content, Electricity-computation-water nexus, Data center dispatch, End-to-end learning, Differentiable optimization, Fixed-point coordination

I. INTRODUCTION

The ongoing process of digitalization is reshaping modern societies through the widespread adoption of smart devices, cloud-based services, and globally interconnected computing infrastructures [1], [2]. This transformation has given rise to a rapidly expanding global digital economy characterized by massive data generation and processing demand. The recent emergence of artificial intelligence (AI), particularly large language models (LLMs), has intensified this trajectory due to their enormous computational requirements [3]. Meeting these demands necessitates the deployment of large-scale data centers (DCs) on an unprecedented scale. According to the International Energy Agency (IEA), global DC electricity demand is set to more than double to around 945 TWh by 2030 [4]. This demand is growing at nearly 12% annually and already accounts for approximately 1.5% of global electricity consumption [5]–[8]. While the electricity implications of this

digital growth are widely studied, its impact on water resources has recently attracted systematic attention.

Beyond direct cooling requirements, DC operations involve water withdrawals embedded in power system operation. The expansion of DC electricity demand driven by these digital trends has led to a substantial increase in water withdrawals [9]. Global DC operations currently withdraw up to 1.7 billion liters of water per day including direct on-site usage and indirect water consumption [10]–[12]. However, understanding the full scope of this water impact requires moving beyond direct consumption metrics. The relationship between DC operations and water resources operates through multiple interconnected layers, necessitating a modeling framework that reflects both grid physics and spatial water dynamics, and that can quantify their impacts on regional water withdrawal patterns. Characterizing the interdependence between power system operation and water redistribution requires a modeling framework that reflects both grid physics and spatial water dynamics. As illustrated in Fig. 1, these interactions manifest as a multi-layer electricity–computation–water (ECW) nexus. At the top layer, computing workload transfers between data centers alter regional electricity demand. These changes trigger cross regional power exchanges within the middle-layer transmission network. The resulting adjustments in generation dispatch reshape water withdrawal patterns in the bottom layer and redistribute the virtual water embodied in power flows [13]. The hierarchy in Fig. 1 reveals that water-related impacts exhibit a progressive scaling effect. Associated water footprint estimates expand from the direct footprint of DCs (10^7 m³/year) to the broader redistribution enabled by the power grid (10^9 m³/year) and finally to the regional water footprint driven by large scale withdrawals (10^{10} m³/year). This process links digital operations with physical resource flows and highlights the necessity of integrated ECW modeling.

Quantifying these grid mediated water impacts requires a framework that can trace water withdrawals from generation sites to end use consumption. Prior studies utilize the virtual water framework to characterize these embedded impacts. Virtual water represents water resources embedded during electricity generation and transferred across the power grid from production sites to consumption regions [14]–[17]. Within this framework, the power grid serves as a physical medium to transfer water-related environmental burdens from generation sites to end-use consumption points [18]–[20]. Exist-

ing research applies multi-regional input-output models [21]–[23] and node flow formulations [24]–[28] to quantify these transfers [20], [29], [30]. However, these accounting-based methods are inherently retrospective because VWC intensities are calculated only after generation schedules and power flows are realized. Consequently, these metrics remain decoupled from real time operational decision making [31], [32]. This structural separation creates a fundamental limitation where data centers possess significant spatial flexibility but dispatch frameworks do not incorporate water-related signals into load allocation. Virtual water analysis remains a descriptive tool and cannot guide proactive optimization decisions during system operations.

To bridge this gap between retrospective accounting and operational coordination, establishing explicit coupling between virtual water metrics and dispatch decision-making becomes essential. Conventional approaches calculate virtual water intensities after dispatch solutions are realized, treating these as independent sequential processes. The power system first optimizes electricity flows to minimize generation costs, and water metrics are subsequently computed based on the resulting generation mix. This separation prevents water-related signals from influencing workload allocation because the intensities used to guide decisions remain fixed at pre-calculated values. However, any reallocation of data center workloads alters regional electricity demand patterns, triggering adjustments in cross regional power exchanges and generation dispatch. These changes reshape the spatial distribution of water withdrawals and modify the virtual water content embodied in power flows. The fundamental challenge is that water intensities depend on dispatch outcomes, while optimal dispatch should ideally reflect water considerations. This creates a circular dependency: water intensities depend on dispatch outcomes, while water-aware dispatch requires knowing these intensities in advance. Resolving this circular dependency necessitates a framework where dispatch optimization and virtual water determination evolve jointly rather than statically.

To resolve this circular dependency, this study develops a learning based framework that embeds dispatch optimization as a differentiable optimization layer within an end-to-end learning architecture [33], [34]. Through the implicit function theorem [35], gradients can be computed and propagated through this differentiable layer. The neural network outputs are projected onto the feasible set, and physical constraints are preserved [36]–[39]. This enables the joint evolution of dispatch decisions and virtual water intensities. These gradients establish computational pathways through which changes in DC workload distribution propagate across the transmission network to affect regional water withdrawal patterns. The resulting framework allows water-related signals to actively guide coordination decisions through gradient-based learning, shifting computational burden from real-time operations to offline training. Building on this differentiable structure, a fixed-point coordination procedure is introduced to iteratively reconcile dispatch solutions with virtual water intensities [40]. Each iteration updates dispatch decisions based on current water signals and recalculates intensities based on realized generation patterns. This iterative process continues until elec-

tricity flows and water withdrawals reach mutual consistency. The resulting framework enables virtual water metrics to transition from retrospective accounting tools to operational coordination signals that actively inform workload allocation decisions.

The main contributions of this study are summarized below.

- A coordination framework is developed within the ECW nexus that integrates DC workload scheduling with virtual water aware dispatch. This framework enables water-related environmental impacts to inform operational decisions rather than serve solely as retrospective metrics.
- A coordination framework is developed that embeds dispatch optimization as a differentiable layer within a learning architecture. Using the implicit function theorem, gradients can be computed and propagated through this layer, enabling end-to-end learning of coordination policies and the joint evolution of dispatch decisions and virtual water intensities, while establishing direct computational pathways from workload allocation to regional water footprints.
- A fixed-point coordination algorithm is introduced to resolve the circular dependency between dispatch outcomes and virtual water intensities. This iterative procedure reconciles electricity flows with water withdrawal patterns until convergence is achieved.

Numerical experiments on representative test systems demonstrate that the proposed framework with differentiable optimization layers and fixed-point coordination reliably resolves the circular dependency between virtual water intensities and dispatch outcomes while maintaining exact consistency between virtual and physical water accounting. Unlike conventional decoupled approaches, the framework enables water-related signals to actively guide workload allocation and generation scheduling through gradient-based learning. The resulting model provides a scalable and operationally grounded foundation for incorporating water-related considerations into power system operation under the continued expansion of digital infrastructure.

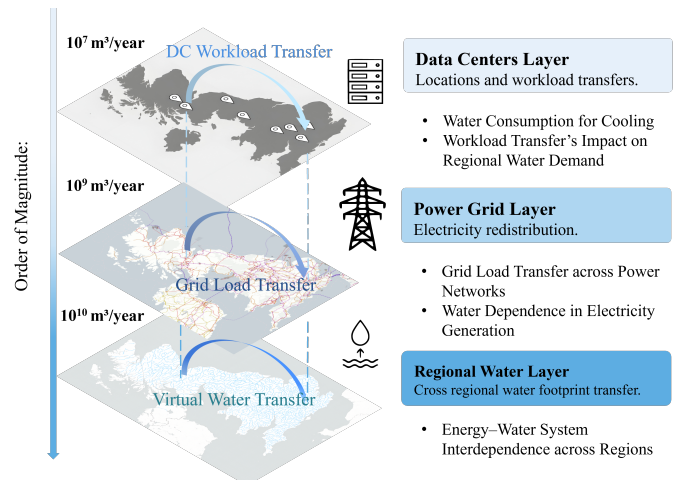


Fig. 1: ECW nexus framework.

II. ECW NEXUS SYSTEM MODELING

To enable coordinated dispatch, this section provides the formal mathematical representation of the ECW nexus. We define a composite objective function to internalize water-related impacts into power system decision making. The section then details the physical and operational constraints governing virtual water flows, data center migrations, and network constrained electricity dispatch.

A. Overall Optimization Formulation

An optimization framework is developed to coordinate power system dispatch, spatial workload allocation, and water scarcity considerations within a unified decision making setting. The formulation seeks generation schedules and workload allocations that balance economic efficiency, water sustainability, and operational stability. This objective is realized by minimizing a composite cost function that accounts for electricity generation costs, virtual water impacts, and workload migration penalties:

$$\min C^{\text{gen}} + C^{\text{water}} + C^{\text{reg}}, \quad (1)$$

where the three components are defined as:

$$C^{\text{gen}} = \sum_{g \in \mathcal{G}} C_g(P_g), \quad (2a)$$

$$C^{\text{water}} = \lambda_w \sum_{n \in \mathcal{N}} \text{VWC}_n \tilde{P}_n, \quad (2b)$$

$$C^{\text{reg}} = \frac{\rho^{\text{mig}}}{2} \sum_{d \in \mathcal{D}} \sum_{n \in \mathcal{N}} (\hat{w}_{d,n} - w_{d,n})^2. \quad (2c)$$

The term C^{gen} captures the operating cost of conventional electricity generation. The term C^{water} internalizes the water-related environmental impact by weighting the effective nodal electricity demand \tilde{P}_n with the corresponding nodal virtual water content VWC_n . The regularization term C^{reg} quantifies the cost of workload reallocation by penalizing deviations of the realized workload allocation $\hat{w}_{d,n}$ from the baseline allocation $w_{d,n}$.

In addition to the objective function, explicit constraints are imposed to represent limits on physical water withdrawals. The water withdrawal for electricity generation at node n is defined as

$$W_n^{\text{gen}} = \sum_{g \in \mathcal{G}_n} \kappa_g P_g, \quad \forall n \in \mathcal{N}. \quad (3)$$

where κ_g is the water withdrawal coefficient of generator g . To reflect system-level water scarcity, a scarcity-weighted water budget is enforced:

$$\sum_{n \in \mathcal{N}} s_n W_n^{\text{gen}} \leq W^{\text{budget}}, \quad (4)$$

where s_n denotes the water stress coefficient at node n and W^{budget} is the total allowable withdrawal.

The optimization is further constrained by the models described in the following subsections. These include the virtual water balance in Eq. (5), the DC workload allocation and Quality of Service constraints in Eq. (6)–(15), and the power system operational constraints in Eq. (18).

This formulation exhibits a circular dependency: C^{water} depends on VWC_n , which is determined by dispatch outcomes through Eq. (5). Section III-A develops an iterative procedure to resolve this coupling.

B. Virtual Water Content of Electricity Consumption

The nodal VWC_n represents the average water withdrawal intensity of electricity demand at bus n , calculated by dividing the total virtual water inflow by the local electricity consumption. Under the proportional sharing principle [41], the virtual water content of incoming flows is traced back to upstream generation sources, with each node's VWC reflecting the weighted average of its supply mix. Accordingly, the nodal virtual water balance is written as

$$\text{VWC}_n = \frac{\sum_{g \in \mathcal{G}_n} \kappa_g P_g + \sum_{m: (m,n) \in \mathcal{L}} \text{VWC}_m [f_{mn}]^+}{\tilde{P}_n}, \quad (5)$$

where $[f_{mn}]^+ = \max(f_{mn}, 0)$ represents incoming power flow from bus m to bus n . The denominator \tilde{P}_n is the effective nodal electricity demand, including both baseline load and DC-induced load, and therefore varies with workload allocation decisions.

Equation (5) shows that virtual water content depends on generation dispatch and network power flows. At the same time, generation and flows are determined by minimizing an objective function that contains VWC_n . This mutual dependence between virtual water content and operational decisions creates a circular coupling that cannot be resolved through standard single-stage optimization, motivating the iterative coordination framework developed in Section III-A.

C. DC Workload Integration

DCs are connected to a subset of transmission buses $d \in \mathcal{D} \subseteq \mathcal{N}$ and are treated as electricity intensive loads. Each bus n generates computing workload δ_n , expressed in electricity equivalent units, part of which can be spatially redistributed among DCs.

Let $w_{d,n}$ denote the portion of workload from bus n that is initially assigned to DC d . The baseline allocation satisfies

$$\sum_{d \in \mathcal{D}} w_{d,n} = \delta_n, \quad \forall n \in \mathcal{N}, \quad (6)$$

$$\sum_{n \in \mathcal{N}} w_{d,n} = \vartheta_d, \quad \forall d \in \mathcal{D}, \quad (7)$$

where ϑ_d is the initial total workload assigned to DC d .

Workload migration is modeled using a virtual transfer network with flow vector ϕ and incidence matrix A^{DC} . The realized workload $\hat{\vartheta}_d$ must satisfy

$$A^{\text{DC}} \phi = \hat{\vartheta} - \vartheta, \quad (8)$$

with capacity limits

$$-\bar{\Phi}_k \leq \phi_k \leq \bar{\Phi}_k, \quad \forall k \in \mathcal{K}^{\text{DC}}. \quad (9)$$

To describe the composition of migrated workload, let $\hat{w}_{d,n}$ denote the portion of workload from bus n that is eventually processed at DC d . It satisfies

$$\sum_{n \in \mathcal{N}} \hat{w}_{d,n} = \hat{\vartheta}_d, \quad \forall d \in \mathcal{D}, \quad (10)$$

$$\sum_{d \in \mathcal{D}} \hat{w}_{d,n} = \delta_n, \quad \forall n \in \mathcal{N}, \quad (11)$$

$$\hat{w}_{d,n} \geq 0, \quad \forall d \in \mathcal{D}, n \in \mathcal{N}. \quad (12)$$

Consistency with aggregate migration is enforced by

$$\sum_{n \in \mathcal{N}} \hat{w}_{d,n} - \sum_{n \in \mathcal{N}} w_{d,n} = [A^{\text{DC}} \phi]_d, \quad \forall d \in \mathcal{D}. \quad (13)$$

To limit service degradation, a latency-based Quality of Service constraint is imposed. The latency coefficient $C_{d,n}$ is defined based on geographical distance between regions, and L^{nom} represents the baseline latency under initial allocation. The realized latency

$$L = \sum_{d \in \mathcal{D}} \sum_{n \in \mathcal{N}} C_{d,n} \hat{w}_{d,n} \quad (14)$$

must satisfy

$$L \leq (1 + \alpha^{\text{QoS}}) L^{\text{nom}}. \quad (15)$$

Each DC converts workload into electricity demand using coefficient Γ_d , so that the DC-induced nodal load is

$$P_n^{\text{DC}} = \sum_{d \in \mathcal{D}_n} \Gamma_d \hat{\vartheta}_d, \quad \forall n \in \mathcal{N}. \quad (16)$$

D. Power System Operational Constraints

The power system is modeled as a steady-state network-constrained dispatch problem. The total nodal electricity demand is

$$\tilde{P}_n = P_n^{\text{base}} + P_n^{\text{DC}}, \quad \forall n \in \mathcal{N}. \quad (17)$$

The operational constraints are

$$\sum_{g \in \mathcal{G}_n} P_g - \tilde{P}_n = \sum_{m \in \Omega_n} b_{nm}(\theta_n - \theta_m), \quad (18a)$$

$$-\bar{F}_{nm} \leq b_{nm}(\theta_n - \theta_m) \leq \bar{F}_{nm}, \quad \forall (n, m) \in \mathcal{L}, \quad (18b)$$

$$\underline{P}_g \leq P_g \leq \bar{P}_g, \quad \forall g \in \mathcal{G}, \quad (18c)$$

$$\theta_{n_0} = 0. \quad (18d)$$

Here P_g is the output of generator g , θ_n is the voltage angle at bus n , b_{nm} is the susceptance of line (n, m) , and \bar{F}_{nm} is its capacity limit. Bus n_0 is the reference bus.

III. DIFFERENTIABLE ELECTRICITY-COMPUTATION-WATER NEXUS FRAMEWORK

The optimization problem in Section II-A involves a circular dependency between generation dispatch and virtual water content through the VWC balance (5). This section develops a learning-based computational framework to resolve this dependency across varying operational scenarios. Section III-A introduces a learning architecture that integrates neural network modules with a differentiable optimization layer. Section III-B presents an iterative procedure that coordinates dispatch decisions with virtual water content values.

A. Differentiable Optimization Layer

The optimization problem formulated in Section II-A exhibits a circular dependency through the VWC balance (5): nodal VWC values depend on generation dispatch and power flows, while dispatch decisions are influenced by VWC through the water-related cost term (2b). Conventional approaches compute dispatch first, then calculate VWC as a post-hoc metric. This sequential treatment prevents water-related signals from guiding dispatch decisions, as VWC values remain fixed during optimization and do not reflect how workload reallocation would alter generation patterns.

To resolve this circular dependency, the dispatch optimization is embedded as a differentiable layer within the learning-based coordination framework. Through the implicit function theorem, gradients of the operational objective backpropagate through the dispatch constraints. This enables workload allocation decisions to account for their downstream effects on generation dispatch, power flows, and water withdrawals.

The framework adopts a learning architecture that integrates neural network modules with a differentiable optimization layer as illustrated in Fig. 2. A multi layer perceptron f_ψ predicts initial generator dispatch from effective nodal demand:

$$\hat{P}_g = f_\psi(\tilde{P}). \quad (19)$$

This prediction accelerates convergence across repeated scenarios but may violate operational constraints. Feasibility is enforced by projecting \hat{P}_g onto the constraint set through a differentiable optimization layer:

$$\begin{aligned} \min \quad & \sum_{g \in \mathcal{G}} (P_g - \hat{P}_g)^2 \\ \text{s.t.} \quad & \text{Constraints (18a)–(18d), (6)–(7),} \\ & \text{(8)–(9), (10)–(12),} \\ & \text{(13), (15), (5), (4).} \end{aligned} \quad (20)$$

In this correction step, VWC_n is treated as fixed and provided by the iterative procedure in Section III-B. Under fixed VWC_n , problem (20) defines a convex program that can be efficiently solved and differentiated.

The optimization layer is implemented as a differentiable convex program [42]. Gradients are obtained by implicit differentiation of the KKT conditions. Appendix A provides the derivation for the QP instance used in our formulation.

These gradients reveal how changes in workload allocation propagate through dispatch decisions to affect water withdrawals. Specifically, a change in $\hat{w}_{d,n}$ alters effective demand \tilde{P}_n , triggering adjustments in generation dispatch P_g and power flows f_{nm} , which in turn modify the water-related cost C^{water} through (2b).

Training minimizes the loss function:

$$\mathcal{L}(\psi) = \mathbb{E}[C^{\text{gen}} + C^{\text{water}} + C^{\text{reg}}] + \lambda_{\text{acc}} \mathbb{E} \left[\left\| \hat{P}_g - P_g^* \right\|_2^2 \right], \quad (21)$$

where P_g^* is the feasible dispatch from (20). The first term captures operational costs including generation, water impacts, and workload migration penalties. The second term with weight $\lambda_{\text{acc}} > 0$ encourages accurate predictions. Gradients

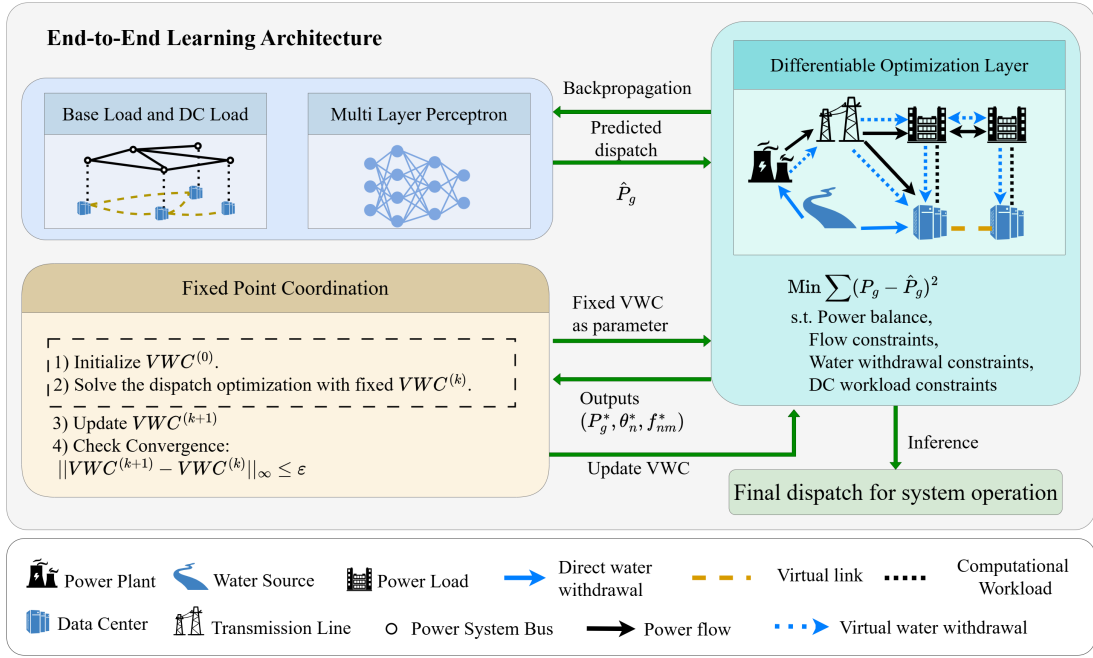


Fig. 2: Overview of the coordination framework with differentiable optimization layers and fixed-point iteration.

of C^{water} flow through the differentiable layer, allowing the predictor to learn policies that reduce water withdrawals by directing computing demand toward regions with lower-intensity generation.

The differentiable architecture shifts VWC from a retrospective accounting tool to an operational signal. After each correction step, the VWC balance (5) is evaluated to update VWC_n , which then influences the next iteration through (2b). This iterative process, detailed in Section III-B, reconciles dispatch decisions with virtual water intensities until convergence is achieved.

B. Iterative Coordination for Endogenous Virtual Water Content

This architecture introduced in Section III-A treats nodal virtual water content values VWC_n as fixed parameters when solving the correction problem (20). This treatment enables the differentiable layer to enforce all operational constraints while maintaining differentiability. However, the virtual water content is not an exogenous system parameter but an endogenous quantity that must be determined consistently with the realized generation dispatch and power flow patterns.

As defined in (5), the virtual water content at each bus depends on the generation dispatch \tilde{P}_g , the power flows f_{nm} , and the effective nodal demand \tilde{P}_n . At the same time, virtual water content values enter the operational objective through the water-related cost term (2b), thereby influencing dispatch decisions. This circular dependence necessitates an iterative procedure in which dispatch decisions and nodal virtual water content values are updated sequentially until mutual consistency is achieved.

Given an estimate $VWC^{(k)} = \{VWC_n^{(k)}\}_{n \in \mathcal{N}}$ at iteration k , the correction problem (20) is solved with $VWC^{(k)}$

treated as fixed, yielding a dispatch and voltage angle solution $\{P_g^{(k)}, \theta_n^{(k)}\}$. The corresponding power flows are computed from the voltage angles as $f_{nm}^{(k)} = b_{nm}(\theta_n^{(k)} - \theta_m^{(k)})$. The nodal virtual water content values are then updated by evaluating the virtual water balance (5) under the resulting dispatch and flows, producing a revised estimate $VWC^{(k+1)}$.

This procedure defines a fixed-point iteration

$$VWC^{(k+1)} = T(VWC^{(k)}), \quad (22)$$

where the operator T implicitly encapsulates solving (20) followed by evaluating (5). A fixed point of this mapping corresponds to a solution in which the virtual water content values used in the dispatch optimization are consistent with those implied by the resulting generation and power flow patterns.

To improve numerical stability, a damped update scheme is applied,

$$VWC^{(k+1)} = \alpha T(VWC^{(k)}) + (1 - \alpha) VWC^{(k)}, \quad \alpha \in (0, 1), \quad (23)$$

which moderates successive updates. The iteration terminates when

$$\|VWC^{(k+1)} - VWC^{(k)}\|_{\infty} < \epsilon, \quad (24)$$

where $\epsilon > 0$ is a prescribed tolerance.

IV. CASE STUDIES

This section evaluates the proposed electricity–computation–water coordination framework through numerical studies on two test systems. Section IV-A examines the IEEE 30-bus network to assess system-level effects under realistic transmission topology and spatially heterogeneous water

scarcity, with particular attention to dispatch patterns, virtual water redistribution, and sensitivity to key parameters. Section IV-B demonstrates scalability of the framework on the IEEE 118-bus system. Sections IV-C and IV-D then consider a 5-bus system to examine convergence behavior of the fixed-point iteration and to verify consistency between virtual and physical water accounting.

A. Analysis on the IEEE 30-Bus System

The proposed framework is evaluated on the IEEE 30-bus system, which includes six generators and heterogeneous nodal loads. Generator water withdrawal coefficients are specified according to regional technology characteristics and range from 2.2 to 2.6 m³/MWh. The scarcity-weighted system-level water constraint (4) is enforced with W^{budget} set to 9000 m³/h. The capacity of each virtual workload migration link is set to $\bar{\Phi}_k = 20$ MW (electricity-load equivalent). Transmission limits follow the standard IEEE 30-bus configuration.

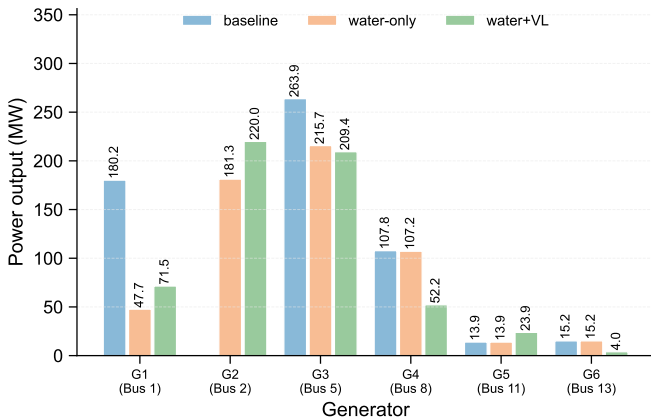


Fig. 3: Generator dispatch across baseline, water-only, and Water+VL configurations.

Fig. 3 reports generator dispatch under three configurations: a baseline case without water considerations, a water-only case with water-related constraints but no workload migration, and a coordinated case with both water constraints and virtual links (Water+VL). In the baseline case, generation is concentrated at large units located at Buses 1 and 5, while smaller generators at Buses 11 and 13 provide limited output. Introducing the system-level water constraint shifts dispatch toward lower-intensity generators. Allowing workload migration further modifies the dispatch pattern: output from the generator at Bus 5 decreases from 263.9 MW to 209.4 MW, while generation at Bus 2 increases to 220.0 MW.

Table I summarizes aggregate system quantities and workload migration patterns under the Water+VL configuration. Total electricity generation remains unchanged, while coordinated operation reduces generation-related water withdrawals by 4.3%. The reconciliation between virtual water consumption and physical water withdrawals is preserved, with $\sum_n \text{VWC}_n \hat{P}_n = \sum_n W_n^{\text{gen}}$, where W_n^{gen} is defined in (3). Workloads are primarily transferred from Buses 8, 23, 27, and 30 toward Buses 1 and 2. Bus 8 exhibits the largest transfers,

TABLE I: System performance and workload transfers under Water+VL configuration on the IEEE 30-bus system.

System-level generation and water withdrawal			
Case	Generation (MW)	Water withdrawal (m ³ /h)	Change (%)
Baseline	580.97	1368.21	–
Water+VL	580.97	1309.16	–4.3

Workload transfers under Water+VL			
Origin Bus	To Bus 1 (MW)	To Bus 2 (MW)	Total (MW)
Bus 8	7.6	8.4	16.0
Bus 23	5.3	4.8	10.1
Bus 27	4.2	4.6	8.8
Bus 30	2.4	2.6	5.0
Total received	19.5	20.4	39.9

with 8.4 MW directed to Bus 2 and 7.6 MW to Bus 1. In total, Bus 2 receives 20.4 MW while Bus 1 receives 19.5 MW. This asymmetric pattern reflects the influence of the virtual water weighted cost term in (2b), which incentivizes allocation of flexible computing demand toward regions supplied by lower-intensity generation.

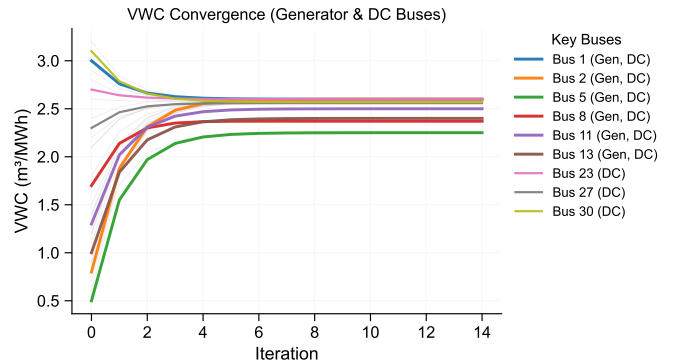


Fig. 4: Convergence of virtual water content during fixed-point iteration.

The fixed-point iteration converges within 10–12 iterations. Across all buses, the converged virtual water content lies between 2.3 and 2.7 m³/MWh, consistent with the range of generator water intensities. Nodes with local generation exhibit VWC values close to their corresponding κ_g , while demand-dominated nodes reflect blended contributions from multiple supply sources through transmission and workload migration.

Fig. 5 compares the spatial distribution of nodal virtual water content under the water-only and Water+VL configurations. Allowing workload migration reduces VWC at several data center buses, including Buses 6, 20, 21, 25, 26, 27, and 29. In the water-only case, VWC at these buses ranges from 2.40 to 2.56 m³/MWh, whereas coordinated operation alleviates these values by redistributing electricity demand away from water-intensive supply regions.

Fig. 6 summarizes system responses. As W^{budget} is increased, the objective value rises and becomes insensitive beyond approximately 9,000 m³/h. Increasing the coefficient λ_w in the virtual-water-weighted cost term (2b) reduces total

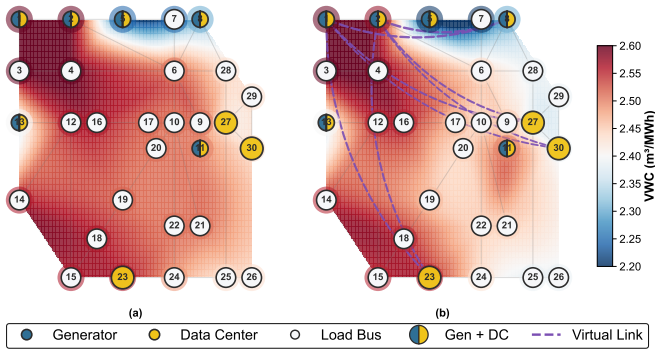


Fig. 5: Spatial distribution of virtual water content under (a) Water+VL and (b) water-only configurations.

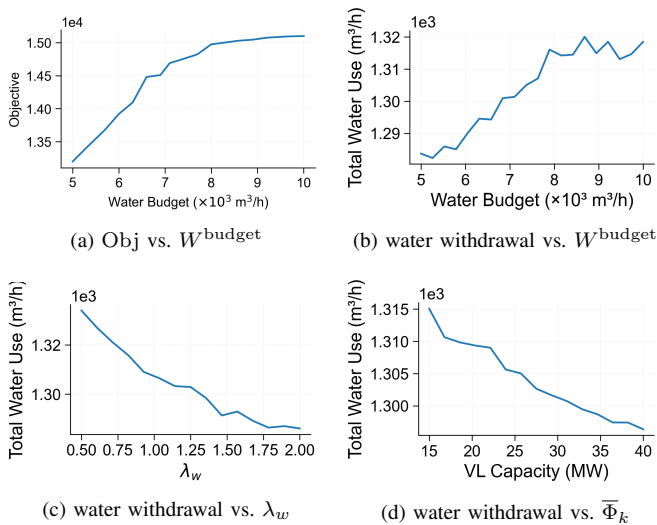


Fig. 6: Sensitivity of system performance to W^{budget} , λ_w , and $\bar{\Phi}_k$.

water withdrawal, while expanding $\bar{\Phi}_k$ yields diminishing returns beyond approximately 25 MW.

B. Scalability Analysis on the IEEE 118-Bus System

TABLE II: Data center workload redistribution on the IEEE 118-bus system.

DC	Bus	Baseline (MW)	Optimized (MW)	Change (MW)
DC1	60	97.5	122.6	+25.1
DC2	78	88.9	93.1	+4.2
DC3	11	82.7	84.5	+1.8
DC4	82	95.8	71.4	-24.4
DC5	45	92.6	69.3	-23.3
DC6	88	73.2	90.7	+17.5
DC7	75	76.4	78.5	+2.1
DC8	106	63.8	75.7	+11.9
DC9	95	78.6	64.2	-14.4
DC10	3	56.2	55.7	-0.5
Total	-	805.7	805.7	0.0

Table II shows data center workload distributions before and after coordinated operation on the IEEE 118-bus system.

TABLE III: System-level comparison on the IEEE 118-bus system.

Metric	Optimized	No Coordination	Change (%)
Total Generation (MW)	4855.04	4854.95	-0.002
Load Shedding (MW)	3.36	3.44	-2.41
Generation Water (m ³ /h)	7662.20	8060.64	-5.20
Total Objective	388,492	407,989	-4.78

Aggregate computing demand remains unchanged at 805.7 MW, while substantial spatial redistribution is observed across data centers. Workloads increase at sites such as DC1 (Bus 60, +25.1 MW) and DC6 (Bus 88, +17.5 MW), and decrease at DC4 (Bus 82, -24.4 MW) and DC5 (Bus 45, -23.3 MW). The redistribution pattern reflects the framework's ability to shift computing demand toward regions with lower water intensity generation while maintaining system-wide workload balance.

Table III compares coordinated and uncoordinated operation. Total electricity generation remains essentially unchanged, while generation-related water withdrawals are reduced by approximately 5.2%. Load shedding is slightly lower under coordinated operation. The reduction in water withdrawal results from spatial reallocation of flexible computing demand toward regions supplied by lower-intensity generation.

C. Convergence Analysis and Water Balance Verification

The fixed-point iteration is examined on a 5-bus test system to assess its convergence behavior and to verify consistency between virtual and physical water accounting. The compact network size allows detailed inspection of nodal quantities and transparent visualization of the iterative process. The system consists of five buses, four generators located at Buses 1, 2, 4, and 5, and four transmission lines. Each generator has a maximum capacity of 400 MW, and each transmission line $(n, m) \in \mathcal{L}$ is subject to a thermal limit of 300 MW. Generator marginal costs are set to (20.0, 25.0, 21.0, 25.0) \$/MWh, and water withdrawal coefficients are $\kappa_g = (3.80, 3.20, 2.60, 2.30)$ m³/MWh for the units at Buses 1, 2, 4, and 5, respectively.

To initialize the iteration, the nodal virtual water content VWC_n is drawn from a uniform distribution over $[2.0, 10.0]$ m³/MWh. This choice allows convergence to be examined from heterogeneous initial conditions without bias toward any specific spatial water-use pattern.

Fig. 7 illustrates the convergence behavior of the fixed-point iteration through two complementary perspectives. Panel (a) demonstrates convergence from heterogeneous initial conditions across all buses in the 5-bus system. Starting from arbitrary initial values, the iteration converges within 6–12 steps, with all buses satisfying the convergence tolerance $\epsilon = 10^{-6}$. Differences in convergence trajectories reflect heterogeneity in network connectivity and generation characteristics. Bus 1, which hosts the most water-intensive generator ($\kappa_g = 3.80$ m³/MWh), attains the highest equilibrium VWC of approximately 3.80 m³/MWh. In contrast, Bus 4, associated

with a low-intensity generator ($\kappa_g = 2.60 \text{ m}^3/\text{MWh}$), converges to the lowest value of approximately $2.60 \text{ m}^3/\text{MWh}$. The smooth and monotonic evolution across all buses indicates stable numerical behavior of the fixed-point mapping under arbitrary initialization.

Panel (b) examines the impact of the damping factor α on convergence dynamics at Bus 1. Five damping factors $\alpha \in \{0.2, 0.4, 0.6, 0.8, 1.0\}$ are evaluated, all starting from a fixed initial value of approximately $5.0 \text{ m}^3/\text{MWh}$. The damping factor significantly influences both convergence speed and trajectory characteristics. Smaller values of α yield slower but smoother convergence trajectories. For instance, $\alpha = 0.2$ requires approximately 18–20 iterations to approach the equilibrium value of approximately $2.75 \text{ m}^3/\text{MWh}$, exhibiting gradual monotonic descent without oscillation. As α increases to 0.4 and 0.6, convergence accelerates progressively while maintaining well-damped behavior. The case $\alpha = 0.6$ reaches equilibrium within 8–10 iterations, demonstrating a favorable balance between speed and numerical stability. At the other extreme, $\alpha = 1.0$ represents undamped updating and converges most rapidly in approximately 2–3 iterations, though this comes at the expense of trajectory smoothness in the early stages. The selection of $\alpha = 0.6$ as the default damping parameter throughout this study is motivated by its ability to achieve reasonably fast convergence without sacrificing numerical stability. Notably, all damping factors converge to the same equilibrium value of approximately $2.75 \text{ m}^3/\text{MWh}$, confirming that the fixed point is independent of the damping schedule and determined solely by the underlying power system structure and generator characteristics.

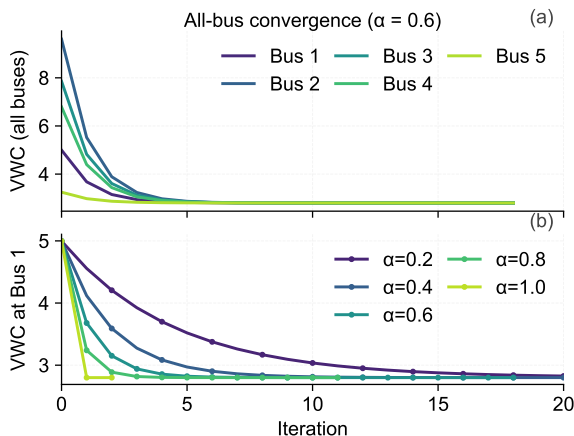


Fig. 7: Convergence of nodal virtual water content under the fixed-point iteration: (a) heterogeneous initial conditions across all buses ($\alpha = 0.6$, $\epsilon = 10^{-6}$); (b) sensitivity to damping factor α at Bus 1.

Table IV reports nodal dispatch outcomes and the corresponding reconciliation between virtual and physical water withdrawals. Total virtual water consumption, computed as $\sum_{n \in \mathcal{N}} \text{VWC}_n \tilde{P}_n$, equals $3148.59 \text{ m}^3/\text{h}$. The total physical water withdrawal, $\sum_{n \in \mathcal{N}} W_n^{\text{gen}}$ with W_n^{gen} defined in (3), equals $3148.58 \text{ m}^3/\text{h}$. The discrepancy of $0.01 \text{ m}^3/\text{h}$ (0.0003%) is attributable to numerical rounding. In this validation case, no

TABLE IV: Node-level reconciliation between virtual and physical water withdrawal.

Bus	\tilde{P}_n (MW)	$P_{g,n}$ (MW)	VWC_{init} (m^3/MWh)	$\text{VWC}_{\text{final}}$ (m^3/MWh)	κ_g	Physical (m^3/h)	
1	200.00	400.00	4.371	3.800	3.80	1520.00	
2	220.00	66.19	9.556	3.651	3.20	211.82	
3	290.00	0.00	7.588	2.753	–	0.00	
4	170.00	400.00	6.388	2.600	2.60	1040.00	
5	150.00	163.81	2.404	2.300	2.30	376.76	
Sum	1030.00	1030.00	–	–	–	3148.58	
Virtual:	$\sum_n \text{VWC}_n \cdot \tilde{P}_n$ (m^3/h)						3148.59

data center workload reallocation is applied, and the effective nodal demand satisfies $\tilde{P}_n = P_{d,n}$ for all buses.

At the nodal level, Bus 1 generates 400 MW using $1520 \text{ m}^3/\text{h}$ of water but serves only 200 MW of local demand, resulting in exports of electricity and its associated embedded water. Bus 3, which has no local generation, imports all of its electricity and exhibits a virtual water footprint determined entirely by upstream sources. These patterns illustrate how nodal virtual water content captures the spatial redistribution of water embodied in electricity flows.

Overall, the fixed-point solution preserves consistency between virtual and physical water accounting, such that the aggregate virtual water embedded in electricity consumption matches total physical withdrawals within numerical tolerance. When nodes host generation with negligible water withdrawal, exported electricity carries correspondingly low embedded water, reducing system-wide water intensity.

D. Coordinated Operation with Water Constraints

This section evaluates coordinated operation on the 5-bus system with water scarcity constraints and workload migration flexibility. Unlike the validation case in Section IV-C, this configuration includes water withdrawal limits and enables spatial workload redistribution. For clarity, the time index t is omitted.

Generators are located at Buses 1, 2, 4, and 5, with water withdrawal coefficients $\kappa_g = 2.8, 0.6, 1.2,$ and $2.3 \text{ m}^3/\text{MWh}$, respectively. The baseline nodal electricity demands are $P_{d,n} = 55.0, 55.0, 62.0, 60.0,$ and 66.0 MW at Buses 1 through 5. The water scarcity weights s_n in (4) are set to 1.5, 2.0, 1.0, 0.5, and 2.0, respectively. The system level scarcity-weighted water constraint (4) is enforced with $W^{\text{budget}} = 5,000 \text{ m}^3/\text{h}$. In addition, nodal water withdrawal capacities are constrained by local water availability, with maximum nodal withdrawals set to $\bar{W}_n^{\text{gen}} = 800, 500, 800, 1200,$ and $600 \text{ m}^3/\text{h}$ at Buses 1 through 5. Each transmission line $(n, m) \in \mathcal{L}$ is subject to a flow limit $\bar{F}_{nm} = 250 \text{ MW}$. Workload migration is enabled with symmetric link capacities $\bar{\Phi}_k = 20 \text{ MW}$. Two configurations are compared. The baseline case excludes water constraints and workload migration. The coordinated case (Water+VL) enforces the system-level water constraint (4) along with nodal water withdrawal limits, and enables workload migration.

In the baseline dispatch, Buses 1 and 4 operate at their maximum limits, while Bus 2 produces 81.79 MW and Bus 5

TABLE V: Node-level water balance: baseline vs. Water+VL operation.

Bus	Baseline (No Coordination)			Water+VL		
	$P_{g,n}$ (MW)	\bar{P}_n (MW)	VWC (m ³ /MWh)	$P_{g,n}$ (MW)	\bar{P}_n (MW)	VWC (m ³ /MWh)
1	400.00	250.00	2.800	400.00	217.70	3.046
2	81.79	190.00	2.024	130.00	190.00	1.762
3	0.00	240.00	1.473	0.00	252.30	1.360
4	400.00	230.00	1.200	400.00	230.00	1.200
5	283.21	255.00	2.300	235.00	275.00	2.187
Total	1165.00	1165.00	-	1165.00	1165.00	-
System water withdrawal (m ³ /h): 2300.46 → 2218.50 (-3.6%)						

produces 283.21 MW. Under coordinated operation, generation shifts toward the water-efficient unit at Bus 2, which increases to 130.00 MW, while generation at Bus 5 decreases to 235.00 MW. Buses 1 and 4 remain capacity-constrained.

Table V shows that nodal virtual water content varies across the network due to differences in local generation and imported electricity. Under coordinated operation, workload migration alters the effective demand pattern, which shifts dispatch toward the low- κ_g generator at Bus 2 and reduces total water withdrawal by 3.6%. At the nodal level, VWC adjusts consistently with the induced changes in physical power flows.

V. CONCLUSION

This paper develops a learning-based coordination framework that embeds dispatch optimization as a differentiable layer, enabling virtual water considerations to directly inform electricity dispatch decisions. By treating virtual water content as an endogenous outcome of dispatch and power flows, the framework allows water scarcity considerations to inform system operation through end-to-end learning rather than retrospective statistical accounting. Numerical studies on IEEE 30-bus and 118-bus systems show that coordinated workload relocation reduces generation-related water withdrawals by 3–5% while preserving power balance and network feasibility. Flexible computing demand shifts electricity consumption toward regions with lower water-intensity generation, thereby alleviating localized water stress without changing aggregate system load. Sensitivity analysis further indicates that the effectiveness of coordination depends on water availability signals and network constraints, with diminishing returns once transmission and generation limits become binding. At the algorithmic level, the fixed-point procedure guarantees consistency between virtual and physical water accounting. Validation on a 5-bus system confirms that virtual water at consumption nodes matches physical withdrawals at generation sites within numerical tolerance. Overall, the proposed framework provides a tractable learning-based approach for integrating virtual water dynamics into power system operations and offers a foundation for coordinated ECW management in systems with growing data center penetration.

APPENDIX

This section derives the backward pass of the optimization layer by implicit differentiation of the KKT conditions.

The optimization layer solves the quadratic program

$$z^* = \arg \min_z \frac{1}{2} z^T Q z + q^T z \quad \text{s.t. } Az = b, Gz \leq h. \quad (25)$$

Let (z^*, ν^*, λ^*) denote the primal and dual optimal variables. The KKT conditions are

$$\begin{aligned} Qz^* + q + A^T \nu^* + G^T \lambda^* &= 0, \\ Az^* - b &= 0, \\ D(\lambda^*)(Gz^* - h) &= 0. \end{aligned} \quad (26)$$

Taking the total differential of the KKT system at the optimum yields a linear system in $(dz, d\lambda, d\nu)$:

$$\begin{aligned} \begin{bmatrix} Q & G^T & A^T \\ D(\lambda^*)G & D(Gz^* - h) & 0 \\ A & 0 & 0 \end{bmatrix} \begin{bmatrix} dz \\ d\lambda \\ d\nu \end{bmatrix} \\ = - \begin{bmatrix} dQz^* + dq + dG^T \lambda^* + dA^T \nu^* \\ D(\lambda^*)dGz^* - D(\lambda^*)dh \\ dAz^* - db \end{bmatrix}. \end{aligned} \quad (27)$$

In the backward pass, given the loss gradient $\partial l / \partial z^*$, we solve for the adjoint variables (d_z, d_λ, d_ν) using the transposed KKT system:

$$\begin{bmatrix} d_z \\ d_\lambda \\ d_\nu \end{bmatrix} = - \begin{bmatrix} Q & G^T D(\lambda^*) & A^T \\ G & D(Gz^* - h) & 0 \\ A & 0 & 0 \end{bmatrix}^{-1} \begin{bmatrix} (\frac{\partial l}{\partial z^*})^T \\ 0 \\ 0 \end{bmatrix}. \quad (28)$$

The gradients with respect to the problem parameters are then given by

$$\begin{aligned} \nabla_Q l &= \frac{1}{2} (d_z z^{*T} + z^* d_z^T), & \nabla_q l &= d_z, \\ \nabla_A l &= d_\nu z^{*T} + \nu^* d_\nu^T, & \nabla_b l &= -d_\nu, \\ \nabla_G l &= D(\lambda^*) d_\lambda z^{*T} + \lambda^* d_\lambda^T, & \nabla_h l &= -D(\lambda^*) d_\lambda. \end{aligned} \quad (29)$$

REFERENCES

- [1] A. Raihan, "A review of the potential opportunities and challenges of the digital economy for sustainability," *Innovation and Green Development*, vol. 3, no. 4, p. 100174, 2024.
- [2] C. G. Bocean and A. A. Vărzaru, "Eu countries' digital transformation, economic performance, and sustainability analysis," *Humanities and Social Sciences Communications*, vol. 10, no. 1, pp. 1–15, 2023.
- [3] J. Ruan, G. Liang, H. Zhao, G. Liu, X. Sun, J. Qiu, Z. Xu, F. Wen, and Z. Y. Dong, "Applying large language models to power systems: Potential security threats," *IEEE transactions on smart grid*, vol. 15, no. 3, pp. 3333–3336, 2024.
- [4] International Energy Agency, "Energy and AI," International Energy Agency, Paris, Tech. Rep., 2025.
- [5] Nature Editorial, "Data centres will use twice as much energy by 2030 — driven by AI," *Nature*, 2025.
- [6] N. Bashir, "Explained: Generative AI's environmental impact," MIT News, 2025.
- [7] A. de Vries, "The growing energy footprint of artificial intelligence," *Joule*, vol. 7, no. 10, pp. 2191–2194, 2023.
- [8] J. Farfan and A. Lohrmann, "Gone with the clouds: Estimating the electricity and water footprint of digital data services in europe," *Energy Conversion and Management*, vol. 290, p. 117225, 2023.
- [9] D. Yates, J. Szinai, and A. Jones, "Modeling the water systems of the western us to support climate-resilient electricity system planning," *Earth's Future*, vol. 12, no. 1, p. e2022EF003220, 2024.
- [10] D. Mytton, "Data centre water consumption," *npj Clean Water*, vol. 4, no. 1, p. 11, 2021.
- [11] N. Lei, J. Lu, A. Shehabi, and E. Masanet, "The water use of data center workloads: A review and assessment of key determinants," *Resources, Conservation and Recycling*, vol. 219, p. 108310, 2025.

- [12] M. A. B. Siddik, A. Shehabi, P. Rao, and L. T. Marston, "Spatially and temporally detailed water and carbon footprints of us electricity generation and use," *Water Resources Research*, vol. 60, no. 12, p. e2024WR038350, 2024.
- [13] W. Zhang, L. A. Roald, A. A. Chien, J. R. Birge, and V. M. Zavala, "Flexibility from networks of data centers: A market clearing formulation with virtual links," *Electric Power Systems Research*, vol. 189, p. 106723, 2020.
- [14] C. M. Chini, L. A. Djehdian, W. N. Lubega, and A. S. Stillwell, "Virtual water transfers of the us electric grid," *Nature Energy*, vol. 3, no. 12, pp. 1115–1123, 2018.
- [15] N. Hogade and S. Pasricha, "A survey on machine learning for geo-distributed cloud data center management," *IEEE Transactions on Sustainable Computing*, vol. 8, no. 1, pp. 15–31, 2022.
- [16] P. Zhao, C. Gu, Z. Cao, Q. Ai, Y. Xiang, T. Ding, X. Lu, X. Chen, and S. Li, "Water-energy nexus management for power systems," *IEEE Transactions on Power Systems*, vol. 36, no. 3, pp. 2542–2554, 2020.
- [17] C. M. Chini and A. S. Stillwell, "The changing virtual water trade network of the european electric grid," *Applied Energy*, vol. 260, p. 114151, 2020.
- [18] P. Tian, H. Lu, H. Reinout, D. Li, K. Zhang, and Y. Yang, "Water-energy-carbon nexus in china's intra and inter-regional trade," *Science of the Total Environment*, vol. 806, p. 150666, 2022.
- [19] X. Liao, X. Zhao, J. W. Hall, and D. Guan, "Categorising virtual water transfers through china's electric power sector," *Applied Energy*, vol. 226, pp. 252–260, 2018.
- [20] Y. Jin and et al., "Virtual water transfer through physical power transmission: Evidence from china, 2006–2022," *Energy*, 2025, in press.
- [21] X. Liao, C. M. Chini, and A. S. Stillwell, "Categorising virtual water transfers through electricity transmission in china," *Applied Energy*, vol. 210, pp. 1244–1256, 2018.
- [22] Y. Guo and et al., "Ecological network analysis for virtual water trade in china's electricity sector," *Ecological Modelling*, vol. 337, pp. 102–110, 2016.
- [23] L. Lin, Y. D. Chen, D. Hua, Y. Liu, and M. Yan, "Provincial virtual energy-water use and its flows within china: A multiregional input-output approach," *Resources, Conservation and Recycling*, vol. 151, p. 104486, 2019.
- [24] X. Zhu, R. Guo, B. Chen, J. Zhang, T. Hayat, and A. Alsaedi, "Embodiment of virtual water of power generation in the electric power system in china," *Applied Energy*, vol. 151, pp. 109–115, 2015.
- [25] C. Zhang and et al., "A node-flow model for virtual water transfers in china's interprovincial electricity trade," *Renewable and Sustainable Energy Reviews*, vol. 73, pp. 376–388, 2017.
- [26] J. Liu, Z. Xu, J. Wu, K. Liu, X. Sun, and X. Guan, "Optimal planning of internet data centers decarbonized by hydrogen-water-based energy systems," *IEEE Transactions on Automation Science and Engineering*, vol. 20, no. 3, pp. 1577–1590, 2022.
- [27] H. Wan, W. Liu, Q. Shi, R. Zhu, X. Zhang, and J. Zhao, "Real-time service restoration of coupled power-water systems considering the spatio-temporal cascading failure," *IEEE Transactions on Smart Grid*, 2025.
- [28] Z. Alnahhal, M. F. Shaaban, M. A. Hamouda, T. Majozi, and M. Al Bardan, "A water-energy nexus approach for the co-optimization of electric and water systems," *IEEE Access*, vol. 11, pp. 28 762–28 770, 2023.
- [29] Y. Zhang, S. Hou, S. Chen, H. Long, J. Liu, and J. Wang, "Tracking flows and network dynamics of virtual water in electricity transmission across china," *Renewable and Sustainable Energy Reviews*, vol. 137, p. 110475, 2021.
- [30] L. Wang, Y. Van Fan, P. Jiang, P. S. Varbanov, and J. J. Klemeš, "Virtual water and co2 emission footprints embodied in power trade: Eu-27," *Energy Policy*, vol. 155, p. 112348, 2021.
- [31] P. Li, X. Liu, Y. Wang, and et al., "Making ai less "thirsty": Uncovering and addressing the secret water footprint of ai models," *arXiv preprint arXiv:2304.03271*, 2023.
- [32] IEA 4E Technology Collaboration Programme, "Data centre energy use: Critical review of models and results," International Energy Agency, Tech. Rep., 2025.
- [33] B. Amos and J. Z. Kolter, "Optnet: Differentiable optimization as a layer in neural networks," in *International conference on machine learning*. PMLR, 2017, pp. 136–145.
- [34] J. Liang, W. Jiang, C. Lu, and C. Wu, "Joint chance-constrained unit commitment: Statistically feasible robust optimization with learning-to-optimize acceleration," *IEEE Transactions on Power Systems*, vol. 39, no. 5, pp. 6508–6521, 2024.
- [35] S. G. Krantz and H. R. Parks, *The implicit function theorem: history, theory, and applications*. Springer Science & Business Media, 2002.
- [36] B. Taheri, R. K. Gupta, and D. K. Molzahn, "Optimizing parameters of the lindistflow power flow approximation for distribution systems," *IEEE Transactions on Smart Grid*, pp. 1–1, 2025.
- [37] P. L. Donti, D. Rolnick, and J. Z. Kolter, "Dc3: A learning method for optimization with hard constraints," in *International Conference on Learning Representations (ICLR)*, 2021.
- [38] A. Agrawal, B. Amos, S. Barratt, S. Boyd, S. Diamond, and J. Z. Kolter, "Differentiable convex optimization layers," *Advances in neural information processing systems*, vol. 32, 2019.
- [39] M. Li, S. Kolouri, and J. Mohammadi, "Learning to solve optimization problems with hard linear constraints," *IEEE Access*, vol. 11, pp. 59 995–60 004, 2023.
- [40] F. Safdarian, O. Ciftci, and A. Kargarian, "A time decomposition and coordination strategy for power system multi-interval operation," in *2018 IEEE Power & Energy Society General Meeting (PESGM)*. IEEE, 2018, pp. 1–5.
- [41] J. W. Bialek and P. A. Kattuman, "Proportional sharing assumption in tracing methodology," *IEE Proceedings-Generation, Transmission and Distribution*, vol. 151, no. 4, pp. 526–532, 2004.
- [42] A. Agrawal, B. Amos, S. Barratt, S. Boyd, S. Diamond, and J. Z. Kolter, "Differentiable convex optimization layers," in *Advances in Neural Information Processing Systems (NeurIPS)*, vol. 32, 2019, pp. 9558–9570.